# Tracking Ultrafast Photocurrents in the Weyl Semimetal TaAs Using THz Emission Spectroscopy

N. Sirica,[1,*] R. I. Tobey,[1,2] L. X. Zhao,[3] G. F. Chen,[3] B. Xu,[3] R. Yang,[3] B. Shen,[4] D. A. Yarotski,[1] P. Bowlan,[1] S. A. Trugman,[1] J.-X. Zhu,[1] Y. M. Dai,[1,5] A. K. Azad,[1] N. Ni,[4] X. G. Qiu,[3] A. J. Taylor,[1] and R. P. Prasankumar[1,†]

[1]*Center for Integrated Nanotechnologies, Los Alamos National Laboratory, Los Alamos, New Mexico 87545, USA*

[2]*Zernike Institute for Advanced Materials, University of Groningen, Groningen 9747AG, Netherlands*

[3]*Institute of Physics, Chinese Academy of Sciences, Beijing 100190, China*

[4]*Department of Physics and Astronomy and California NanoSystems Institute, University of California Los Angeles, Los Angeles, California 90095, USA*

[5]*School of Physics, Nanjing University, Nanjing 210093, China*

(Received 1 November 2018; revised manuscript received 5 February 2019; published 15 May 2019)

We investigate polarization-dependent ultrafast photocurrents in the Weyl semimetal TaAs using terahertz (THz) emission spectroscopy. Our results reveal that highly directional, transient photocurrents are generated along the noncentrosymmetric $c$ axis regardless of incident light polarization, while helicity-dependent photocurrents are excited within the $ab$ plane. This is consistent with earlier static photocurrent experiments, and demonstrates on the basis of both the physical constraints imposed by symmetry and the temporal dynamics intrinsic to current generation and decay that optically induced photocurrents in TaAs are inherent to the underlying crystal symmetry of the transition metal monopnictide family of Weyl semimetals.

DOI: 10.1103/PhysRevLett.122.197401

*Introduction.*—The recent prediction and subsequent discovery of Weyl fermions as emergent quasiparticles in materials possessing strong spin-orbit interaction and broken time-reversal or inversion symmetry has generated substantial interest, due to their fundamental and technological relevance [1–5]. A defining characteristic of the electronic structure of these Weyl semimetals (WSMs) is the existence of Weyl points, where nondegenerate, linearly dispersing bands found in the bulk of these materials cross [6–10]. These points act as monopoles of Berry curvature in momentum space and are found to be topologically stable even in the absence of any particular symmetry [6,7]. This leads to several unique experimental manifestations of Weyl physics, including Fermi arcs [8–11] and the chiral anomaly [12–14].

Linear optical spectroscopy has revealed novel phenomena in WSMs, including the predicted linear scaling of conductivity with frequency and strong Weyl fermion-phonon coupling [15–17]. Further insight into Weyl physics can be gained from nonlinear optics through the effect that Berry curvature introduces on such nonlinear quantities as the shift vector and photocurrent [18,19]. Specifically, for noncentrosymmetric WSMs, like the transition metal monopnictides (TMMPs), the shift vector, which defines a difference in the center of electron charge density within one unit cell following optical excitation [20], develops a contribution arising from a change in Berry curvature between the bands participating in the transition [18]. This behavior has been studied in the TMMPs, where a giant anisotropic nonlinear response was observed in the optical and near-infrared (IR) range [21,22]. The dominant contribution to the nonlinear response measured along the polar $c$ axis was attributed to a helicity-independent shift current originating from the strong polar character of these materials [22,23]. However, polarization-dependent photocurrent measurements made on WSMs following mid-IR excitation have suggested a topologically nontrivial contribution to the shift current, revealing a colossal bulk photovoltaic effect that may be linked to divergent Berry curvature near the Weyl nodes [24,25].

Helicity-dependent photocurrents measured in topological insulators [26,27] and WSMs [28–30] have likewise provided insight into their topologically nontrivial behavior. The direction of these photocurrents can be switched by changing light helicity (i.e., degree of circular polarization), potentially enabling all-optical control without an external bias field. In WSMs, the contribution of injection currents, which result from an asymmetric distribution of carriers in momentum space due to the interference of different light polarizations [20], to the circular photogalvanic effect (CPGE) drives a helicity-dependent photocurrent that is claimed to provide a direct experimental measure for the topological charge of Weyl points [28,31–33]. Experimentally, the CPGE was demonstrated in static photocurrent measurements of the WSM TaAs following mid-IR and optical excitation [28,29], and was subsequently used to determine Weyl fermion chirality based upon the direction that current flows relative to the high symmetry axes of the crystal. Despite their observation of a helicity-dependent photocurrent, Ref. [28] reported a negligible

 

contribution from shift currents. This finding contrasts with that in Ref. [24], raising the question of why static photocurrent measurements made on the same WSM reveal such different results.

In this Letter, we demonstrate the generation of both helicity-dependent and helicity-independent ultrafast photocurrents as measured by terahertz (THz) emission spectroscopy on the WSM TaAs. THz emission, detected either directly though electro-optic sampling (EOS) or by THz field-induced second-harmonic generation (TFISH), is a contact-free means of measuring transient photocurrents on the intrinsic timescales that underlie their generation and decay [34]. Despite our use of femtosecond near-IR optical pulses to drive these photocurrents, our results agree well with previous static photocurrent measurements, and have the added advantage that photothermal effects are largely mitigated due to the ultrashort duration of the driving pulse. Below, we will focus on the results obtained from TaAs, but the same behavior is observed for the closely related TMMP WSM NbAs (Fig. S1) [35].

*Experiment.*—THz emission from a 1-mm-thick as-grown TaAs single crystal was measured using an amplified Ti:sapphire laser system operating at a 1 kHz repetition rate. Ultrashort optical pulses centered at 800 nm (1.55 eV) with a duration of ~40 femtoseconds (fs) and fluences up to 17 $\mathrm{mJ/cm^2}$ were incident on the crystal surface, and the specularly emitted THz radiation was detected by free space EOS in a 0.5-mm-thick $\langle 110 \rangle$ ZnTe crystal (Fig. S2) [35]. Measurements were made on the (001) and (112) faces at both ~5° and ~45° angles of incidence. The (112) surface, which has been the subject of previous investigations [21,22], possesses two in-plane, high symmetry axes, $[1\,\bar{1}\,0]$ and $[1\,1\,\bar{1}]$ (Fig. S2), where the latter contains a projection of the inversion symmetry-broken $c$ axis. A wire grid polarizer was used to determine the polarization of the emitted THz pulses relative to these crystal axes. Finally, all experiments were performed at room temperature in an enclosure purged with dry air.

*Results and discussion.*—Our main results are shown in Fig. 1, which illustrates in both Figs. 1(a) and 1(b) a clear polarity reversal of the emitted THz waveform polarized along the $[1\,\bar{1}\,0]$ axis, occurring as the helicity of the optical generation pulse is tuned from left circular to right circular polarization [36]. Analysis of the THz waveforms in Fig. 1 shows a 180° polarity reversal, with no variation in frequency, and a change in amplitude that corresponds to the degree of ellipticity of the incident light pulse. A plot of the peak-to-peak amplitude of the emitted THz electric ($E$) field while rotating the $\lambda/4$ wave plate (QWP) over a full 360° reveals a sinusoidal dependence whose periodicity matches a change in helicity of the incident light [Fig. 1(c)]. Fitting with a general expression for the polarization dependence of the photocurrent [26],

$$j(\alpha) = C \sin 2\alpha + L_1 \sin 4\alpha + L_2 \cos 4\alpha + D, \quad (1)$$

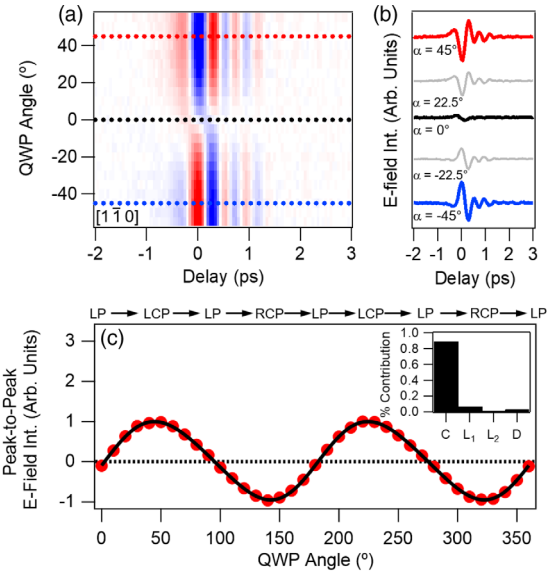


FIG. 1. (a) False color plot and (b) select time-dependent THz traces, illustrating the polarity reversal of the emitted THz waveform upon changing the helicity of the optical generation pulse. Traces shown in (b) are obtained using quarter wave plate (QWP) angles of ±45°, ±22.5°, and 0°, which correspond to right or left circular, elliptical, or linear polarizations, respectively. (c) Peak-to-peak $E$-field amplitude plotted as a function of $\alpha$ and fit with Eq. (1). The inset illustrates the relative weight of each fitting component.

where $\alpha$ is the QWP angle, reveals the dominant (~90%) contribution to arise from the helicity-dependent term, $C$. However, the emitted THz pulse is strongly suppressed, but not entirely quenched, when the polarization of the incident light is linear [Fig. 1(b)]. This implies a small deviation of ~7% from the ideal $\sin 2\alpha$ behavior, which is due to the helicity-independent, but linearly dependent term $L_1$, as well as an ~3% contribution from the polarization-independent term $D$. Further investigation into the linearly-dependent THz emission reveals a change in both amplitude and phase of the THz waveform as the polarization of the generating pulse is tuned from horizontal to vertical (Fig. S3) [35]. However, since both $L_1$ and $D$ provide only small contributions to the polarization dependence of the emitted THz pulse along the $[1\,\bar{1}\,0]$ axis, we will primarily focus on the dominant, helicity-dependent behavior observed along this high-symmetry direction.

In contrast, THz emission polarized along the $[1\,1\,\bar{1}]$ direction, obtained under the same excitation conditions as above, was found to be largely insensitive to the polarization of incident light, and approximately half as intense as that measured along $[1\,\bar{1}\,0]$. As shown in Fig. 2, no variation in the THz waveform and only a small (<10%) variation in the $E$-field amplitude is observed with rotation of either a $\lambda/4$ or a $\lambda/2$ wave plate (Fig. S4) [35]. Fitting the peak-to-peak amplitude of the THz $E$-field along $[1\,1\,\bar{1}]$ with Eq. (1) shows that the dominant (~90%) contribution derives from $D$, as expected by the large offset shown in the

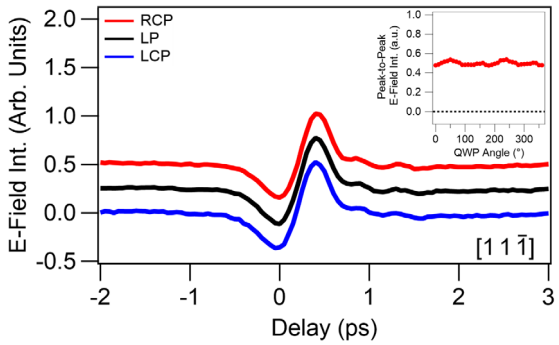


FIG. 2. THz emission spectra measured along the $[1\,1\,\bar{1}]$ axis generated by right circular, linear, and left circularly polarized optical pulses (traces are offset for clarity). The inset shows the peak-to-peak $E$-field amplitude plotted as a function of $\alpha$.

inset of Fig. 2. Despite this polarization insensitivity, the emitted THz radiation is linearly polarized along the $[1\,1\,\bar{1}]$ axis and exhibits a well-defined directionality. This is illustrated by both an azimuthal dependence that shows the amplitude of the helicity-independent THz waveform to peak along this high symmetry direction (Fig. S5) [35], as well as a switching of the emitted THz polarity under a 180° rotation of the crystal [Fig. 3(a)].

Similarly, helicity-dependent THz radiation polarized along the $[1\,\bar{1}\,0]$ axis exhibits a reversal of polarity under a 180° rotation of the sample [Fig. 3(b)]. This shows that the emitted THz radiation is highly directional; however,

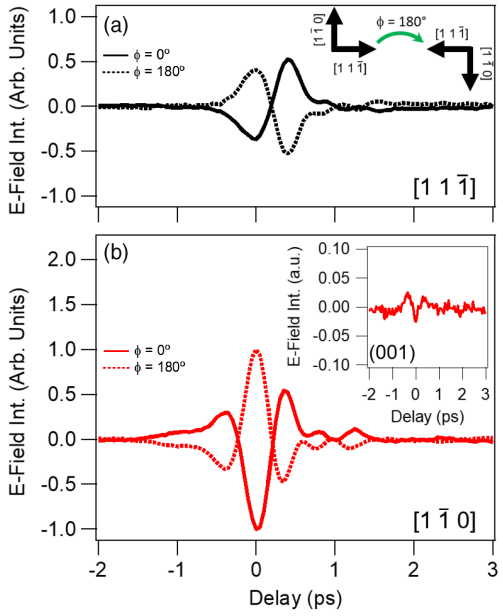


FIG. 3. THz emission spectra measured along (a) $[1\,1\,\bar{1}]$ and (b) $[1\,\bar{1}\,0]$, generated from linearly or right circularly polarized light, respectively. Spectra denoted by dashed lines were obtained following a 180° azimuthal rotation of the TaAs crystal about the (112) normal. The inset in (b) illustrates the helicity-dependent THz waveform emitted along the $[1\,\bar{1}\,0]$ direction from the (001) surface at normal incidence.

unlike Fig. 3(a), the directionality of the THz waveform along this axis is determined by the relative orientation that the optical generation pulse makes with the polar $c$ axis. This is most clearly demonstrated by measuring THz emission along the same $[1\,\bar{1}\,0]$ high symmetry direction, but on the (001) face of the crystal, where the $c$ axis lies parallel to the surface normal. Here, the THz pulse emitted at normal incidence is more than 40 times weaker than that measured from the (112) surface under the same conditions [Fig. 3(b) inset]. However, when repeating the experiment on the (001) face at a 45° angle of incidence, the helicity-dependent THz emission is recovered and qualitatively similar to that found from the (112) face (Fig. S6) [35].

THz pulses emitted along both high symmetry axes of the (112) surface are found to scale linearly with laser fluence and exhibit no change in waveform or frequency content as higher excitation fluences are used (Fig. S7) [35]. By Fourier transforming the THz time-domain traces shown above, one finds the spectral weight of the THz intensity power spectrum along $[1\,1\,\bar{1}]$ to be shifted towards lower frequencies (∼1.0 THz) [Fig. 4(a)], and thus longer timescales, as compared to that of the helicity-dependent THz radiation emitted along $[1\,\bar{1}\,0]$ (Fig. S7) [35]. As it turns out, spectra measured along $[1\,\bar{1}\,0]$ by free space EOS are limited by the detection bandwidth of the $\langle 110\rangle$ ZnTe crystal (Fig. S8) [35,37]. This remains true even when thinner ZnTe crystals are used, making it difficult to accurately estimate the emitted THz bandwidth using this technique.

To provide a better estimate for the bandwidth of the helicity-dependent THz pulse polarized along $[1\,\bar{1}\,0]$, we used TFISH [38]. Here, the sensitivity of optical second-harmonic generation (SHG) to broken inversion symmetry enables us to detect the electric field of the transient THz pulse without the bandwidth limitations imposed by the strong vibrational resonances in electro-optic crystals. More specifically, the THz field emitted after exciting the sample with a circularly polarized 800 nm pump pulse (as in the experiments described above) induces a change in the SHG signal polarized along the in-plane $[1\,\bar{1}\,0]$ direction. This can be measured with a separate probe beam through a $\chi^{(3)}$ process that acts in addition to the usual $\chi^{(2)}$ component. In this way, TFISH can be described as a four-wave mixing process in which light of frequency $2\omega$ is generated from mixing light with frequencies $\omega$, $\omega$, and $\omega_{\mathrm{THz}}$, and represented by the second order electric polarization,

$$P_i(2\omega) = [\chi^{(2)}_{ijk} + \chi^{(3)}_{ijkl} E_l(\omega_{\mathrm{THz}})] E_j(\omega) E_k(\omega), \quad (2)$$

where $\chi^{(3)}$ has the same symmetry constraints as $\chi^{(2)}$, leaving the symmetry of the SHG pattern unchanged.

Time-domain waveforms obtained from our TFISH measurements are shown in the inset of Fig. 4(b), where the emitted THz pulse is isolated after subtracting the longer time dynamics associated with the pump-induced

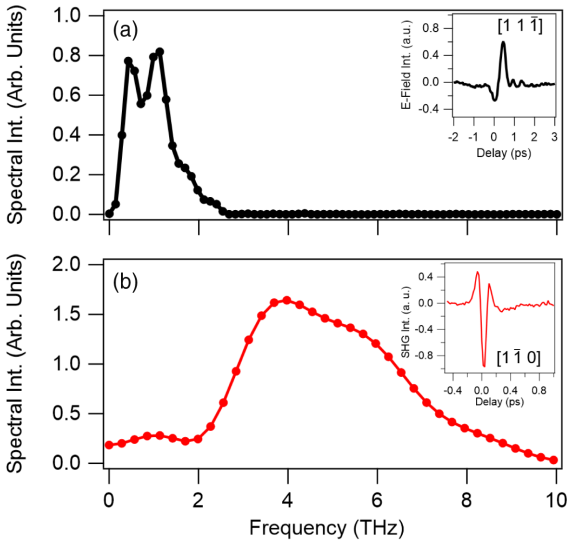


FIG. 4. Intensity power spectra obtained by Fourier transforming (a) time-domain THz waveforms measured along $[1\,1\,\bar{1}]$ using free space EOS (inset) and (b) helicity-and-time-dependent THz pulses measured with TFISH (inset) following appropriate subtraction of the time-resolved SHG dynamics along the $[1\,\bar{1}\,0]$ axis.

change in the SHG signal (Fig. S9) [35,39]. As compared to the THz waveform measured by EOS, the temporal duration of the emitted THz pulse detected by TFISH is significantly shorter, with an intensity power spectrum that yields a bandwidth out to 10 THz [Fig. 4(b)]. While substantially broader than that obtained by free space EOS, even this is limited by the temporal resolution of the time-resolved SHG experiment, meaning that an upper limit of ~100 fs can be placed on the underlying dynamics responsible for the helicity-dependent THz radiation emitted from the TMMP family of WSMs.

From the data presented above, we can conclude that the helicity-dependent THz emission shown in Fig. 1 derives from an ultrafast photocurrent flowing along the $[1\,\bar{1}\,0]$ high symmetry direction. This is consistent with the previously reported CPGE in these materials [28,29], and is further supported by symmetry considerations (Supplemental Material, Sec. X [35,40]). In particular, for circularly polarized light, denoted by the complex $E$-field, $\mathcal{E}$, normally incident on the (112) face, symmetry constraints placed on the CPGE response tensor, $\gamma_{ls}$, by the $C_{4v}$ point group of the crystal allow for a helicity-dependent, transverse photocurrent ($J$) to flow along the $[1\,\bar{1}\,0]$ axis, while forbidding a helicity-dependent photocurrent along $[1\,1\,\bar{1}]$:

$$J^{\mathrm{CPGE}}_{[1\,\bar{1}\,0]} = i\frac{\gamma_{xy}}{\sqrt{3}}(\vec{\mathcal{E}}\times\vec{\mathcal{E}}^{*})_{[112]}$$
$$J^{\mathrm{CPGE}}_{[1\,1\,\bar{1}]} = 0. \qquad (3)$$

Furthermore, as expected from Fig. 3(b), the in-plane photocurrent, $J^{\mathrm{CPGE}}_{[1\,\bar{1}\,0]}$, will necessarily switch sign following a 180° rotation of the crystal, while photocurrent generation from light normally incident on the (001) face is found to be symmetry forbidden (Fig. S6) [35]. Hence, our experimental findings are in complete agreement with what is expected by symmetry for the CPGE. However, before assigning the mechanism underlying helicity-dependent photocurrents to this effect, it is important to note that such photocurrents can also arise from alternate mechanisms, including the circular photon drag effect (CPDE) and spin-galvanic effect (SGE) [41,42].

Transverse helicity-dependent photocurrents originating from the CPDE [43] are allowed under the $C_{4v}$ symmetry of TaAs, but our symmetry analysis (Supplemental Material, Sec. X) [35] shows that these currents flow along the $[1\,1\,\bar{1}]$ axis as opposed to the $[1\,\bar{1}\,0]$ direction. Figure 2 shows that THz emission along $[1\,1\,\bar{1}]$ is largely polarization independent, with a small helicity-dependent contribution, as found from a fit of the peak-to-peak THz amplitude as a function of QWP angle [Fig. S4(a)] [35]. For this reason, the CPDE plays a minor role in the generation of helicity dependent photocurrents in TaAs and can be excluded as a mechanism for generating the dominant ultrafast photocurrent along $[1\,\bar{1}\,0]$ (Fig. 1) [35].

In contrast, distinguishing between a helicity-dependent photocurrent arising from the CPGE versus the SGE requires dynamical insights that can be gained by analysis of the THz waveform. Unlike a nonresonant second order process, the helicity-dependent THz radiation emitted here corresponds to a real, transient current. Consequently, the spectral bandwidth and waveform of the emitted THz pulse are not dependent on that of the excitation pulse, but are intrinsic features of the ultrafast current generated in these materials [34]. For a pulsed excitation, the decay of the helicity-dependent photocurrent will be determined by either the momentum or spin relaxation time, depending upon whether it originates from the CPGE or the SGE [41]. The broad emission bandwidth observed along the $[1\,\bar{1}\,0]$ axis [Fig. 4(b)] implies a lifetime of $<100$ fs for the excited photocurrent. This is more consistent with a current decay following the momentum relaxation time of a free carrier than a slower spin relaxation due to asymmetric spin-flip scattering of photoexcited carriers [41,42]. When coupled with the above symmetry analysis, this leaves the most likely origin of the helicity-dependent photocurrent to be injection photocurrents that give rise to the CPGE.

As compared to the helicity-dependent THz emission observed along the $[1\,\bar{1}\,0]$ axis, the fundamental mechanism underlying THz emission polarized along $[1\,1\,\bar{1}]$ is distinct. Since this axis contains a projection of the inversion symmetry-broken $c$ axis, both the polarization independence and the well-defined directionality of the photocurrent suggest an underlying mechanism rooted in broken inversion symmetry. As a result, THz emission measured along the $[1\,1\,\bar{1}]$ axis of the (112) surface is intrinsic to the noncentrosymmetric crystal structure of TaAs and can

likely be understood as an optical excitation producing electron-hole pairs, regardless of polarization, which are then separated by the dipolelike field of the polar Ta-As bond lying along the $c$ axis. Such a microscopic picture is consistent with that of a shift current [21,22,24].

In this regard, despite our use of femtosecond optical pulses whose energy is well above the energy scale associated with the Weyl cone, the THz emission spectra shown here exhibit the same fundamental behavior as observed in static photocurrent experiments. Despite this similarity, assigning a microscopic mechanism to the ultrafast photocurrents observed in TaAs becomes challenging, as arguments rooted in Weyl physics hold for mid-IR excitation [24,28] but not for optical excitation, where details of the trivial band structure are expected to become more relevant [44]. Rather, our findings suggest that under optical excitation these transient photocurrents are intrinsic to the underlying crystal symmetry of TaAs, whose $C_{4v}$ symmetry belongs to the gyrotropic crystal class, and may not have an explicit link to Weyl physics beyond the fact that such a symmetry supports the existence of Weyl nodes in the electronic structure.

*Conclusion.*—In closing, we performed THz emission spectroscopy on the (112) and (001) surfaces of the TMMP WSM TaAs. Our data enables us to clearly distinguish between helicity-dependent photocurrents generated within the $ab$-plane and polarization-independent photocurrents flowing along the noncentrosymmetric $c$ axis. Such findings are in excellent agreement with previous static photocurrent measurements. However, by considering both the physical constraints imposed by symmetry and the temporal dynamics intrinsic to current generation and decay, we can attribute these transient photocurrents to the underlying crystal symmetry of the TMMP family of WSMs.

This work was performed at the Center for Integrated Nanotechnologies at Los Alamos National Laboratory (LANL), a U.S. Department of Energy, Office of Basic Energy Sciences user facility. N. S. and R. P. P. gratefully acknowledge the support of the U.S. Department of Energy through the LANL LDRD Program and the G. T. Seaborg Institute. D. Y. and J. X. Z. were supported by the Center for Advancement of Topological Semimetals, an Energy Frontier Research Center funded by the U.S. Department of Energy Office of Science, Office of Basic Energy Sciences, through the Ames Laboratory under its Contract No. DE-AC02-07CH11358. R. I. T. was the recipient of the Los Alamos National Laboratory Rosen Scholar Award, supported by LDRD Grant No. 20180661ER. Work at U. C. L. A. was supported by the US DOE, Office of Science, Office of Basic Energy Sciences under Award No. DE-SC0011978.

*nsirica@lanl.gov
†rpprasan@lanl.gov

[1] N. P. Armitage, E. J. Mele, and A. Vishwanath, Rev. Mod. Phys. **90**, 015001 (2018).
[2] M. Hasan, S.-Y. Xu, I. Belopolski, and S. H. Huang, Annu. Rev. Condens. Matter Phys. **8**, 289 (2017).
[3] B. Yan and C. Felser, Annu. Rev. Condens. Matter Phys. **8**, 337 (2017).
[4] S. Jia, S.-Y. Xu, and M. Z. Hasan, Nat. Mater. **15**, 1140 (2016).
[5] Y. Tokura, M. Kawasaki, and N. Nagaosa, Nat. Phys. **13**, 1056 (2017).
[6] G. Xu, H. Weng, Z. Wang, X. Dai, and Z. Fang, Phys. Rev. Lett. **107**, 186806 (2011).
[7] X. Wan, A. M. Turner, A. Vishwanath, and S. Y. Savrasov, Phys. Rev. B **83**, 205101 (2011).
[8] S.-Y. Xu *et al.*, Science **349**, 613 (2015).
[9] B. Q. Lv, N. Xu, H. M. Weng, J. Z. Ma, P. Richard, X. C. Huang, L. X. Zhao, G. F. Chen, C. E. Matt, F. Bisti, V. N. Strocov, J. Mesot, Z. Fang, X. Dai, T. Qian, M. Shi, and H. Ding, Nat. Phys. **11**, 724 (2015).
[10] L. X. Yang, Z. K. Liu, Y. Sun, H. Peng, H. F. Yang, T. Zhang, B. Zhou, Y. Zhang, Y. F. Guo, M. Rahn, D. Prabhakaran, Z. Hussain, S.-K. Mo, C. Felser, B. Yan, and Y. L. Chen, Nat. Phys. **11**, 728 (2015).
[11] Z. K. Liu, L. X. Yang, Y. Sun, T. Zhang, H. Peng, H. F. Yang, C. Chen, Y. Zhang, Y. Guo, D. Prabhakaran, M. Schmidt, Z. Hussain, S.-K. Mo, C. Felser, B. Yan, and Y. L. Chen, Nat. Mater. **15**, 27 (2016).
[12] S. A. Parameswaran, T. Grover, D. A. Abanin, D. A. Pesin, and A. Vishwanath, Phys. Rev. X **4**, 031035 (2014).
[13] X. Huang, L. Zhao, Y. Long, P. Wang, D. Chen, Z. Yang, H. Liang, M. Xue, H. Weng, Z. Fang, X. Dai, and G. Chen, Phys. Rev. X **5**, 031023 (2015).
[14] C.-L. Zhang, Nat. Commun. **7**, 10735 (2016).
[15] B. Xu, Y. M. Dai, L. X. Zhao, K. Wang, R. Yang, W. Zhang, J. Y. Liu, H. Xiao, G. F. Chen, A. J. Taylor, D. A. Yarotski, R. P. Prasankumar, and X. G. Qiu, Phys. Rev. B **93**, 121110 (R) (2016).
[16] B. Xu, Y. M. Dai, L. X. Zhao, K. Wang, R. Yang, W. Zhang, J. Y. Liu, H. Xiao, G. F. Chen, S. A. Trugman, J.-X. Zhu, A. J. Taylor, D. A. Yarotski, R. P. Prasankumar, and X. G. Qiu, Nat. Commun. **8**, 14933 (2017).
[17] S.-i. Kimura, H. Yokoyama, H. Watanabe, J. Sichelschmidt, V. Süß, M. Schmidt, and C. Felser, Phys. Rev. B **96**, 075119 (2017).
[18] T. Morimoto and N. Nagaosa, Sci. Adv. **2**, e1501524 (2016).
[19] T. Morimoto, S. Zhong, J. Orenstein, and J. E. Moore, Phys. Rev. B **94**, 245121 (2016).
[20] J. E. Sipe and A. I. Shkrebtii, Phys. Rev. B **61**, 5337 (2000).
[21] L. Wu, S. Patankar, T. Morimoto, N. L. Nair, E. Thewalt, A. Little, J. G. Analytis, J. E. Moore, and J. Orenstein, Nat. Phys. **13**, 350 (2017).
[22] S. Patankar, L. Wu, B. Lu, M. Rai, J. D. Tran, T. Morimoto, D. E. Parker, A. G. Grushin, N. L. Nair, J. G. Analytis, J. E. Moore, J. Orenstein, and D. H. Torchinsky, Phys. Rev. B **98**, 165113 (2018).
[23] Z. Li, Y.-Q. Jin, T. Tohyama, T. Iitaka, J.-X. Zhang, and H. Su, Phys. Rev. B **97**, 085201 (2018).
[24] G. B. Osterhoudt, L. K. Diebel, X. Yang, J. Stanco, X. Huang, B. Shen, N. Ni, P. Moll, Y. Ran, and K. S. Burch, Nat. Mater. **18**, 471 (2019).

[25] J. Ma, Q. Gu, Y. Liu, J. Lai, Y. Peng, X. Zhuo, Z. Liu, J.-H. Chen, J. Feng, and D. Sun, Nat. Mater. **18**, 476 (2019).
[26] J. W. McIver, D. Hsieh, H. Steinberg, P. Jarillo-Herrero, and N. Gedik, Nat. Nanotechnol. **7**, 96 (2012).
[27] C. Kastl, C. Karnetzky, H. Karl, and A. W. Holleitner, Nat. Commun. **6**, 6617 (2015).
[28] Q. Ma, S.-Y. Xu, C.-K. Chan, C.-L. Zhang, G. Chang, Y. Lin, W. Xie, T. Palacios, H. Lin, S. Jia, P. A. Lee, P. Jarillo-Herrero, and N. Gedik, Nat. Phys. **13**, 842 (2017).
[29] K. Sun, S.-S. Sun, L.-L. Wei, C. Guo, H.-F. Tian, G.-F. Chen, H.-X. Yang, and J.-Q. Li, Chin. Phys. Lett. **34**, 117203 (2017).
[30] Z. Ji, G. Liu, Z. Addison, W. Liu, P. Yu, H. Gao, Z. Liu, A. M. Rappe, C. L. Kane, E. J. Mele, and R. Agarwal, arXiv:1802.04387.
[31] F. de Juan, A. G. Grushin, T. Morimoto, and J. E. Moore, Nat. Commun. **8**, 15995 (2017).
[32] C.-K. Chan, N. H. Lindner, G. Refael, and P. A. Lee, Phys. Rev. B **95**, 041104(R) (2017).
[33] Y. Zhang, H. Ishizuka, J. van den Brink, C. Felser, B. Yan, and N. Nagaosa, Phys. Rev. B **97**, 241118(R) (2018).
[34] J. B. Baxter and C. A. Schmuttenmaer, *Terahertz Spectroscopy Principles and Applications*, edited by S. L. Dexheimer (CRC Press, Boca Raton, 2007), p. 73.
[35] See Supplemental Material at http://link.aps.org/supplemental/10.1103/PhysRevLett.122.197401 for a more detailed discussion of supporting figures and derivations.
[36] All data underlying Figs. 1–4 can be accessed at https://doi.org/10.18126/M28D30.
[37] R. A. Kaindl, *Optical Techniques for Solid-State Materials Characterization*, edited by R. P. Prasankumar and A. J. Taylor (CRC Press, Boca Raton, 2012), p. 397.
[38] A. Nahata and T. F. Heinz, Opt. Lett. **23**, 67 (1998).
[39] Y. M. Sheu, S. A. Trugman, L. Yan, Q. X. Jia, A. J. Taylor, and R. P. Prasankumar, Nat. Commun. **5**, 5832 (2014).
[40] J. Quereda, T. S. Ghiasi, J.-S. You, J. van den Brink, B. J. van Wees, and C. H. van der Wal, Nat. Commun. **9**, 3346 (2018).
[41] S. D. Ganichev and W. Prettl, J. Phys. Condens. Matter **15**, R935 (2003).
[42] S. D. Ganichev, E. L. Ivchenko, V. V. Bel'kov, S. A. Tarasenko, M. Sollinger, D. Weiss, W. Wegscheider, and W. Prettl, Nature (London) **417**, 153 (2002).
[43] V. A. Shalygin, M. D. Moldavskaya, S. N. Danilov, I. I. Farbshtein, and L. E. Golub, Phys. Rev. B **93**, 045207 (2016).
[44] C.-C. Lee, S.-Y. Xu, S.-M. Huang, D. S. Sanchez, I. Belopolski, G. Chang, G. Bian, N. Alidoust, H. Zheng, M. Neupane, B. Wang, A. Bansil, M. Z. Hasan, and H. Lin, Phys. Rev. B **92**, 235104 (2015).